NANO LETTERS
Letter
Cite This: Nano Lett. 2017, 17, 6968-6973
pubs.acs.org/NanoLett

Reduced Magnetism in Core–Shell Magnetite@MOF Composites

Sameh K. Elsaidi,[†,§] Michael A. Sinnwell,[†] Debasis Banerjee,[†] Arun Devaraj,[†] Ravi K. Kukkadapu,[‡] Timothy C. Droubay,[†] Zimin Nie,[⊥] Libor Kovarik,[‡] Murugesan Vijayakumar,[‡] Sandeep Manandhar,[†,∥] Manjula Nandasiri,[‡] B. Peter McGrail,[⊥] and Praveen K. Thallapally*[,†]

[†]Physical and Computational Science Directorate and [‡]Environmental Molecular Sciences Laboratory, Pacific Northwest National Laboratory, Richland, Washington 99352, United States

[§]Chemistry Department, Faculty of Science, Alexandria University, P.O. Box 426, Ibrahimia, Alexandria 21321, Egypt

[∥]Department of Mechanical Engineering, University of Texas at El Paso, El Paso, Texas 79968, United States

[⊥]Energy and Environment Directorate, Pacific Northwest National Laboratory, Richland, Washington 99352, United States

Supporting Information

ABSTRACT: The magnetic susceptibility of synthesized magnetite (Fe_3O_4) microspheres was found to decline after the growth of a metal–organic framework (MOF) shell on the magnetite core. Detailed structural analysis of the core–shell particles using scanning electron microscopy, transmission electron microscopy, atom probe tomography, and ^{57}Fe–Mössbauer spectroscopy suggests that the distribution of MOF precursors inside the magnetic core resulted in the oxidation of the iron oxide core.

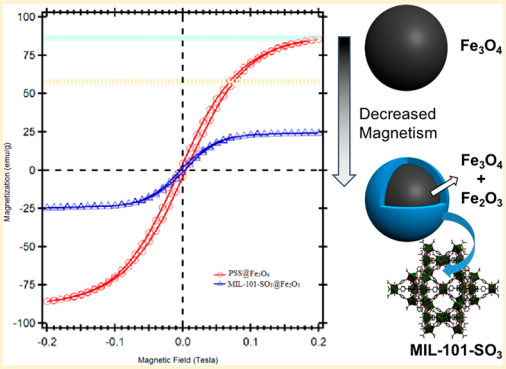

KEYWORDS: *Metal–organic framework, MOF, magnetite, core–shell magnetic microparticle, Mössbauer spectroscopy, atom probe tomography*

Engineered magnetic nanoparticles (MNPs) have emerged as promising materials for technological applications including separations,[1] catalysis,[2] medicine,[3−7] and environmental remediation.[8] In combination with well-established synthetic routes to precisely control the size and morphology of MNPs, surface functionalization offers a way to expand functionality beyond that of the individual particles.[9−11]

In this context, metal–organic frameworks (MOFs), a class of highly porous, crystalline, solid-state materials, are considered a viable candidate "shell" due to inherent synthetic and chemical stability.[12−17] The introduction of a MOF shell over a magnetic core is a promising and intriguing approach for developing a magnetic core–shell composite that can easily be isolated and recovered by the application of an external magnetic field.[18,19] Indeed, MOF–MNP composites have obvious advantages in adsorption and separation and afford a facile strategy to make MOFs highly recyclable by prohibiting significant material loss.[20−34] Therefore, we need to understand how the magnetic properties of the MNPs are affected by the growth of a MOF shell.

Herein, we report a reduction in magnetic susceptibility of magnetite (Fe_3O_4) cores as a result of the oxidative growth of a MOF shell. Well-defined Fe_3O_4 microspheres were synthesized and functionalized with a MIL-101-SO_3 shell (MIL: Materials Institute Lavoisier).[35,36] The shape and morphology of the novel core–shell Fe_3O_4@MOF composite (herein, Fe_3O_4@MIL-101-SO_3) were characterized by scanning and transmission electron microscopy (SEM and TEM, respectively). Atom probe tomography (APT) was conducted to determine the nanoscale distribution of MIL-101-SO_3 within the core–shell particles. Following detailed structural analysis, magnetic saturation experiments demonstrated that the magnetic properties of the Fe_3O_4 cores were affected by surface functionalization.

To generate a core–shell Fe_3O_4@MOF composite, we set out to coat magnetite particles with a water-stable and porous MOF. MIL-101-SO_3 possesses negatively charged sulfonic acid (SO_3^-) groups uniformly distributed on the pore surface. Charge-balanced by Na^+ or H^+ cations,[35] these cations are readily exchangeable, making the material suitable for applications in aqueous separations.[37] Our goal here was to not only probe the magnetic properties of Fe_3O_4@MOF composites but also produce a potentially functional and novel core–shell material.

The core–shell particles were prepared by synthesizing Fe_3O_4 microspheres and functionalizing them with a known

Received: August 12, 2017
Revised: October 9, 2017
Published: October 19, 2017

DOI: 10.1021/acs.nanolett.7b03451
Nano Lett. 2017, 17, 6968–6973

binding agent, poly(sodium 4-styrenesulfonate) (PSS) for a better adherence of the MOF to the surface of the Fe_3O_4 core (Figure 1).[38] In situ solvothermal synthesis techniques were

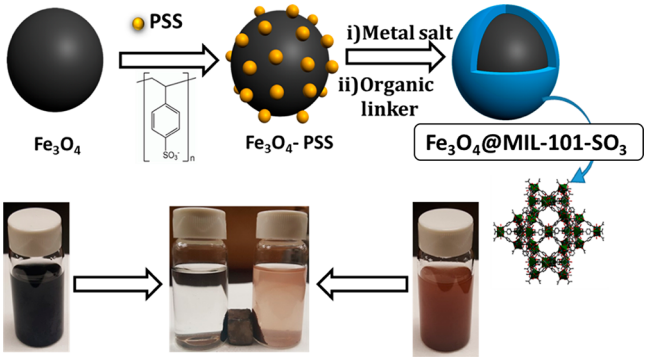

Figure 1. Schematic representation of the Fe_3O_4@MIL-101-SO_3 core formation.

used to coat MIL-101-SO_3 on Fe_3O_4–PSS microspheres (see the Methods section and the Supporting Information). The phase purity, stability, and porosity of the MOF, as-synthesized Fe_3O_4, PSS-functionalized Fe_3O_4, and Fe_3O_4@MIL-101-SO_3 were assessed by powder X-ray diffraction (XRD), thermal gravimetric analysis (TGA), and Brunauer–Emmett–Teller (BET) surface area measurements (see the Methods section and Figure S1–S5). The core–shell particles (376 m^2/g) show significant porosity upon MOF growth compared to the pristine core (6 m^2/g). The improved porosity of the core–shell particles was reflected in the thermogravimetric analysis (TGA), which suggested growth of MOF (~10 wt %) shells around the core particles. The Fe_3O_4@MIL-101-SO_3 can be easily and efficiently removed by the application of an external magnetic field, as shown in Figure 1.

Furthermore, the particle size of the magnetic core and the thickness of the MOF "shell" on its surface were measured and characterized using SEM and TEM techniques (Figure 2). Electron microscopic imaging suggests the pristine Fe_3O_4 microspheres were spherical with an approximate diameter of 300–500 nm. The diameter of the microspheres increases to ~800–900 nm after MOF coating without any change in shape and morphology (Figures 2a–c and S6–S8). TEM and energy dispersive X-ray spectroscopy (EDX) analyses suggest MIL-101 SO_3 has a thickness of 300 nm over the surface of the entire core particle, with a ratio of Cr to Fe of 1:4 by percentage (Figure 2d–g).

To evaluate the extent of nanoscale distribution of MIL-101-SO_3 within the core–shell particle, APT was conducted. APT is an advanced microscopy method capable of providing subnanometer-scale, spatially resolved three-dimensional compositional mapping of materials with sensitivity up to a few parts per million.[39] A single Fe_3O_4@MIL-101-SO_3 particle was chosen and attached to a silicon microtip array holder using electron beam assisted Pt welding (Figure 3a,b).[40] The image

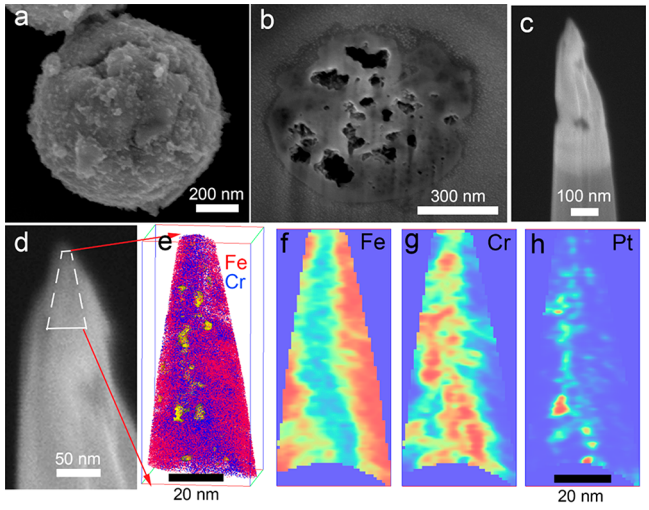

Figure 3. (a) SEM image of one MIL-101-SO_3@Fe_3O_4 microsphere. (b) Cross-section of the same MIL-101-SO_3@Fe_3O_4 microsphere. (c) SEM image of the needle shaped specimen of MIL-101-SO_3@Fe_3O_4. (d) Magnified view of the MIL-101-SO_3@Fe_3O_4 needle apex, where the region analyzed by APT is highlighted by white dashed lines. (e) 3D atom distribution of Fe (red), Cr (blue), and Pt (yellow) in the MIL-101-SO_3H@Fe_3O_4 obtained by APT analysis. 2D compositional maps of an axial slice of the 3D APT data showing elemental distribution of (f) Fe, (g) Cr, and (h) Pt showing their mutually exclusive locations within the MOF particle. The scale bars of all three 3D maps in panels f and g are 20 nm.

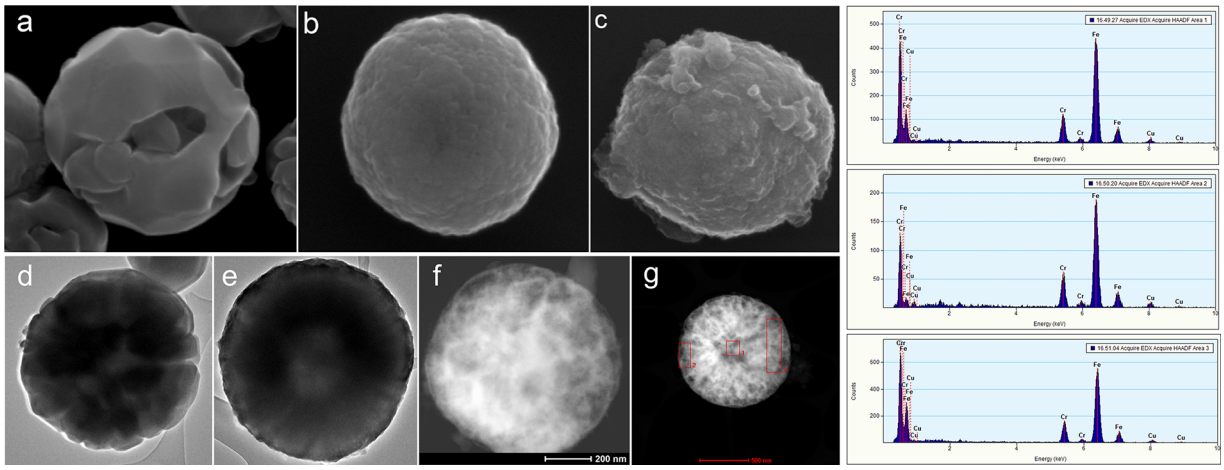

Figure 2. SEM, TEM, and EDX studies of the magnetic core–shell microsphere. (a–c) SEM images of Fe_3O_4, Fe_3O_4–PSS, and Fe_3O_4@MIL-101-SO_3. (d–f) TEM images of Fe_3O_4, Fe_3O_4–PSS, and Fe_3O_4@MIL-101-SO_3. (g) TEM and corresponding EDX data showing elemental composition of Fe_3O_4@MIL-101-SO_3.

DOI: 10.1021/acs.nanolett.7b03451
Nano Lett. 2017, 17, 6968–6973

of the final Fe_3O_4@MIL-101-SO_3 needle specimen is given in Figure 3c. Figure 3d is a magnified image of the specimen apex, with the region analyzed by APT marked with dashed lines. A 40.2 nm × 38.7 nm × 90.2 nm volume from within the particle was analyzed. A three-dimensional (3D) elemental map of the distribution of Fe and Cr is shown in Figure 3e. The pores were identified based on the presence of a high concentration of Pt, which was used to backfill the pores during annular milling. In Figure 3e (Supplementary Video 1), the Fe (red dots) represents the magnetic core, Cr (blue dots) (Supplementary Video 2) corresponds to the MIL-101-SO_3 coating, and Pt (yellow dots) corresponds to pores in the core−shell microsphere (Supplementary Video 3). To view the elemental distribution more clearly, two-dimensional (2D) elemental compositional maps were plotted using a 1 nm slice of the 3D atom probe data; these are shown in Figure 3f−h. The color scale of each 2D elemental map is normalized, with red representing the highest concentration and blue representing the lowest concentration of each element. Figure 3f shows the Fe map, where the presence of Fe is indicated in all regions shown in red. The center region with low Fe corresponds to pores. Figure 3g is the 2D distribution of Cr, situated along the walls of the pores or inside the porous regions. Figure 3h shows the Pt distribution, confirming the presence of pores in those locations. The Cr penetration into the mesoporous Fe_3O_4 microsphere indicates that MOF formed and either partially or entirely filled some pores within the Fe_3O_4 particle or that Cr was trapped during initial MOF synthesis (Supplementary Video 4).

The Fe_3O_4@MIL-101-SO_3 was further characterized by magnetic saturation experiments to investigate their intrinsic magnetic properties. The saturation magnetization (M_s) of pristine Fe_3O_4 and PSS-loaded Fe_3O_4 was found to be 91 emu/g, consistent with literature values.[41] The coercive field (H_c) value was found to be consistent with magnetic particles of >75 nm diameter. The saturation magnetization, M_s, and coercive field of Fe_3O_4@MIL-101-SO_3 were reduced by ∼72% (25 emu/g) as compared to pristine Fe_3O_4 microspheres (Figures 4a and S9). The reduction in M_s has been observed in other Fe_3O_4@MOF composites, but the root cause of the reduction in M_s has not been identified.[19,42,43] The reduction in M_s can be attributed to reductive dissolution of the magnetic core, but as discussed previously, electron microscopic results do not support a reduction in particle size upon MOF coating. An alternative possibility is the partial oxidation of the Fe^{2+} of the Fe_3O_4 core to Fe^{3+} during in situ MOF coating.

To test this possibility, Mössbauer spectroscopy was performed at room temperature on freshly synthesized samples of Fe_3O_4, PSS-grafted Fe_3O_4, and MIL-101-Fe_3O_4@MIL-101-SO_3 (Figure 4b). The Mössbauer spectra clearly indicate the as-synthesized magnetite microsphere has a charge distribution similar to that of $[(Fe^{3+})_{tet}(Fe^{3+}, Fe^{2+})_{oct}]O_4$ based on relative intensities of the sextet peaks. As expected, functionalization with PSS did not result in any change in the oxidation state of the as-synthesized magnetite. However, the Mössbauer spectrum of the Fe_3O_4@MIL-101-SO_3 clearly indicates oxidation of Fe^{2+} to Fe^{3+}; as a result, the magnetite core was converted to maghemite (Fe_2O_3) upon MOF coating. The oxidation is facilitated by high-temperature hydro(solvo) thermal synthesis under aerobic conditions. Complementary synchrotron based X-ray absorption near-edge spectroscopy (XANES) reveals that Fe_3O_4 microspheres and PSS-functionalized Fe_3O_4 and Fe_3O_4 coated with PSS have significant

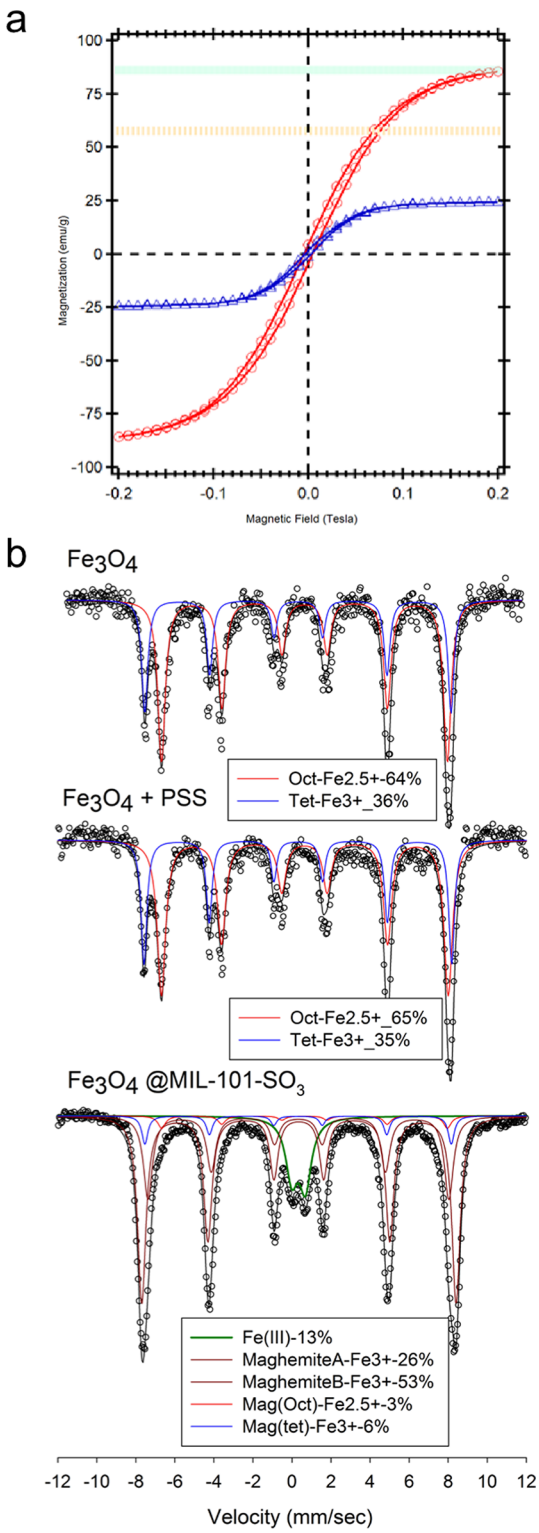

Figure 4. Magnetic saturation and Mössbauer and X-ray absorption spectra. (a) Magnetic saturation of Fe_3O_4−PSS (red) and Fe_3O_4@MIL-101-SO_3 (blue) at room temperature (notice the bulk magnetite (Fe_3O_4) and maghemite (Fe_2O_3) saturation magnetization in light green and orange, respectively). (b) Mössbauer spectral data of Fe_3O_4 (top), Fe_3O_4−PSS (middle), and Fe_3O_4@MIL-101-SO_3 (bottom), indicating the conversion of Fe^{2+} to Fe^{3+} in the magnetic core upon MOF coating.

DOI: 10.1021/acs.nanolett.7b03451
Nano Lett. 2017, 17, 6968−6973

contributions of the Fe^{2+} oxidation state, whereas in Fe_3O_4@MIL-101-SO_3, the Fe oxidation state is dominated by the Fe^{3+} component (Figures 4 and S10).[44]

In summary, important new chemistry in the growth of MOF shell sorbents on magnetite cores has been discovered. We have designed and synthesized novel core−shell Fe_3O_4@MOF microspheres. APT shows that under the given synthesis conditions, deposition of Cr or MOF occurs within the pores of the magnetic core in conjunction with a redox reaction that oxidizes a significant fraction of the Fe^{2+} in the magnetite and reduces its magnetic properties. Here, we have provided fundamental insights into the change MOF growth has on the magnetic properties of Fe_3O_4 cores.

Methods. *General Synthetic Method for Functionalized Magnetic Core.* The Fe_3O_4 core was synthesized by stirring $FeCl_3 \cdot 9H_2O$ and ethylene glycol for 30 min.[45] Sodium acetate in appropriate quantity was added to the dark-yellow solution, and the solution was stirred for another 1 h. The brown solution was then transferred to Teflon-lined Parr autoclaves and heated for 18 h at 200 °C. The black, solid product was separated from the medium using an external magnet and subsequently washed with water (three times) and methanol (three times) and dried in air. After the Fe_3O_4 was synthesized, it was coated with PSS by adding the Fe_3O_4 to a 0.3% aqueous PSS solution, followed by sonication for 1 h.[38] The product was then washed with water and collected using a permanent magnet and characterized by powder XRD (see the Supporting Information).

General Synthesis Procedure of MOF and Core−Shell Magnetic Microspheres. Unbound MIL-101-SO_3 was prepared using a published procedure.[35] MIL-101-SO_3 was grown on the Fe_3O_4−PSS core by mixing CrO_3 with Fe_3O_4−PSS in water, followed by sonication for 1 h. Thereafter the organic linker, monosodium 2-sulfoterephthalic acid, and concentrated HCl were added to the solution, followed by sonication for another 30 min. The resultant solution was then transferred to a Teflon-lined Parr autoclave and heated for 6 days at 180 °C. The magnetic, brown solid of Fe_3O_4@MIL-101-SO_3 was separated using a permanent magnet and washed with water and methanol (3 × 50 mL). The products were characterized by powder XRD, BET surface area, and SEM and TEM measurements (see the Supporting Information for a detailed synthetic scheme).

Microstructural Characterization. The Fe_3O_4@MIL-101-SO_3 was characterized using SEM backscattered electron imaging in an FEI Quanta dual beam, focused ion beam (FIB) system. The TEM samples and APT samples were prepared using the FEI Quanta dual beam FIB. The APT specimen preparation method, by site specific FIB lift-out and annular milling, aided in selecting specific regions within the sample.[46] A CAMECA LEAP 4000XHR system equipped with a pulsed UV laser (355 nm wavelength) was used to perform APT experiments using 20 pJ laser pulse energy and 0.005 atoms per pulse evaporation rate at a specimen temperature of 60 K. The APT results were reconstructed and analyzed using Interactive Visualization and Analysis Software (IVAS) 3.6.8 using a standard reconstruction procedure.[47] The reconstruction and composition measurement of all APT data was done using x−y−z voxels of 1 nm × 1 nm × 1 nm size with a delocalization of 3 × 3 × 1.5 nm, respectively. The error bars for composition measurements were estimated based on statistical error for measured atom count as per the equation below, where C^i corresponds to measured atomic concentration fraction of the element and N is the total atom counts in the bin:

$$\sigma = \sqrt{\frac{C^i*(1 - C^i)}{N}}$$

X-ray Absorption Near-Edge Spectroscopy. All of the samples in the form of powders were pressed into In foil and affixed onto a Cu sample puck using carbon tape. The Fe L-edge, Cr L-edge, and O K-edge X-ray absorption spectra were collected at beamline 6.3.1.2 of the advanced light source (ALS) in total electron yield mode while maintaining the analysis chamber pressure below 1×10^{-9} Torr vacuum. Calibration standards were provided by ALS and mounted within the XAS instrument chamber for accurately calibrating the energy positions.

Electron Microscopy Analysis. Scanning transmission electron microscopy (STEM) measurements were performed with an FEI Titan 80−300 operated at 300 kV. The FEI Titan is equipped with a CEOS GmbH double-hexapole aberration corrector for the probe-forming lens. The STEM images were acquired in high-angle annular dark-field mode with an inner collection angle of 52 mrad. Conventional TEM images were acquired with a Gatan UltraScan 1000 camera. Sample preparation for TEM observations involved mounting powder samples on copper grids covered with lacey carbon support films and then immediately loading them into the STEM airlock. To further confirm the composition of the Fe_3O_4@MIL-101-SO_3 particles, energy dispersive X-ray spectroscopy was performed on several particles, which suggested the distribution of MOF over entire particles; the ratio of Cr to Fe was found to be 20/80.

Magnetometry Measurements. Vibrating sample magnetometry (VSM) measurements were carried out on a Lakeshore 7404 magnetometer at room temperature. Core−shell microspheres were allowed to dry at room temperature to a powder form and then loaded into a powder sample holder. Any small residual ferromagnetic signal from the bare sample holder was subtracted from the total signal. Residual ferromagnetic response was typically <0.1% of the total signal of the samples. M_S values were determined and reported after subtracting the paramagnetic contribution from the signal. A nickel sphere was used to calibrate the magnetometer. Uncertainty in the calibration standard is estimated at ±1.5%. Mössbauer spectroscopy data of the powder samples were collected using a WissEl Elektronik instrument (Germany). A ^{57}Co/Rh source (50-mCi to 75-mCi, initial strength) was used as the γ energy source. The transmitted counts were stored in a multichannel scaler as a function of the energy (transducer velocity) using a 1024-channel analyzer. The raw data were folded to 512 channels to provide a flat background and a zero-velocity position corresponding to the center shift of a metal Fe foil at room temperature. Calibration spectra were obtained with a 20 μm thick Fe foil placed in the same position as the samples to minimize any geometry errors. The Mössbauer spectroscopy data were modeled with Recoil software (University of Ottawa, Canada) using a Voigt-based structural fitting routine.

DOI: 10.1021/acs.nanolett.7b03451
Nano Lett. 2017, 17, 6968−6973

■ ASSOCIATED CONTENT

Supporting Information

The Supporting Information is available free of charge on the ACS Publications website at DOI: 10.1021/acs.nanolett.7b03451.

Additional experimental details and figures on syntheses, powder XRD measurements, TGA, BET surface area analysis, SEM and TEM images, magnetic saturation analysis, and XANES analysis. (PDF)

Video 1: The distribution of Fe in the magnetic core (AVI)

Video 2: The distribution of Cr in the magnetic core (AVI)

Video 3: The distribution of Pt in the magnetic core (AVI)

Video 4: The distribution of Fe, Cr, Pt in the magnetic core (AVI)

■ AUTHOR INFORMATION

Corresponding Author

*E-mail: praveen.thallapally@pnnl.gov.

ORCID

Praveen K. Thallapally: 0000-0001-7814-4467

Author Contributions

S.K.E. performed the synthesis, preparation, and characterization of MOFs and MOF-coated Fe_3O_4 microspheres, powder XRD measurements and ion-exchange studies on MOF core−shell microspheres, data analysis, and the inductively coupled plasma optical emission spectrometry (ICP-OES) calculations. D.B. synthesized and screened unbound MOFs and performed ion-exchange studies. Z.N. performed the ICP-OES study. M.N. and L.K. performed SEM and TEM studies. R.K.K. collected and modeled Mössbauer spectra. T.C.D. performed and analyzed the magnetometry. A.D. and S.M. collected and analyzed the atom probe data. V.M. analyzed the EXAFS data. B.P.M. conceived the original research, and P.K.T. executed it. S.K.E., M.A.S., B.P.M, and P.K.T. wrote the manuscript with input from all authors.

Notes

The authors declare no competing financial interest.

■ ACKNOWLEDGMENTS

We thank the U.S. Department of Energy, Geothermal Technologies Office for supporting this work, especially Timothy Reinhardt, Joshua Mengers, and Holly Thomas for constructive criticism over the course of the Phase I project. A portion of this research (Mössbauer, atom probe, SEM and TEM, and magnetometry) was performed in the Environmental Molecular Sciences Laboratory, a national scientific user facility sponsored by the Department of Energy's Office of Biological and Environmental Research and located at Pacific Northwest National Laboratory (PNNL). The synthesis of the material was supported by the U.S. Department of Energy, Office of Science, Basic Energy Sciences, Division of Materials Sciences and Engineering, under award no. KC020105-FWP12152. PNNL is a multiprogram national laboratory operated for the U.S. Department of Energy by Battelle Memorial Institute under contract no. DE-AC05-76RL01830. The Advanced Light Source is supported by the Director, Office of Science, Office of Basic Energy Sciences, of the U.S. Department of Energy under contract no. DE-AC02-05CH11231.

■ ABBREVIATIONS

MNPs, magnetic nanoparticles; MOF, metal−organic framework; APT, atom probe tomography; SEM, scanning electron microscopy; TEM, transmission electron microscopy; PSS, poly(sodium 4-styrenesulfonate); XRD, X-ray diffraction; BET, Brunauer−Emmett−Teller; XANES, X-ray absorption near-edge spectroscopy; Ms, saturation magnetization; ALS, advanced light source; EDX, energy dispersive X-ray spectroscopy; EXAFS, extended X-ray absorption fine structure; FIB, focused ion beam; MIL, Materials Institute Lavoisier; STEM, scanning transmission electron microscopy; TGA, thermal gravimetric analysis; UV, ultraviolet; VSM, vibrating sample magnetometer; XAS, X-ray absorption spectroscopy

■ REFERENCES

(1) Iranmanesh, M.; Hulliger, J. *Chem. Soc. Rev.* **2017**, *46*, 5925−5934.

(2) Gawande, M. B.; Branco, P. S.; Varma, R. S. *Chem. Soc. Rev.* **2013**, *42*, 3371−3393.

(3) Gupta, A. K.; Gupta, M. *Biomaterials* **2005**, *26*, 3995−4021.

(4) Colombo, M.; Carregal-Romero, S.; Casula, M. F.; Gutierrez, L.; Morales, M. P.; Bohm, I. B.; Heverhagen, J. T.; Prosperi, D.; Parak, W. J. *Chem. Soc. Rev.* **2012**, *41*, 4306−4334.

(5) Reddy, L. H.; Arias, J. L.; Nicolas, J.; Couvreur, P. *Chem. Rev.* **2012**, *112*, 5818−5878.

(6) Sun, C.; Lee, J. S. H.; Zhang, M. *Adv. Drug Delivery Rev.* **2008**, *60*, 1252−1265.

(7) Li, Y.; Zhang, X.; Deng, C. *Chem. Soc. Rev.* **2013**, *42*, 8517−8539.

(8) Jung, J. H.; Lee, J. H.; Shinkai, S. *Chem. Soc. Rev.* **2011**, *40*, 4464−4474.

(9) Wu, L.; Mendoza-Garcia, A.; Li, Q.; Sun, S. *Chem. Rev.* **2016**, *116*, 10473−10512.

(10) Lu, A.-H.; Salabas, E. L.; Schüth, F. *Angew. Chem., Int. Ed.* **2007**, *46*, 1222−1244.

(11) Ghosh Chaudhuri, R.; Paria, S. *Chem. Rev.* **2012**, *112*, 2373−2433.

(12) Yaghi, O. M.; O'Keeffe, M.; Ockwig, N. W.; Chae, H. K.; Eddaoudi, M.; Kim, J. *Nature* **2003**, *423*, 705−714.

(13) Kitaura, R.; Kitagawa, S.; Kubota, Y.; Kobayashi, T. C.; Kindo, K.; Mita, Y.; Matsuo, A.; Kobayashi, M.; Chang, H.-C.; Ozawa, T. C.; Suzuki, M.; Sakata, M.; Takata, M. *Science* **2002**, *298*, 2358−2361.

(14) Férey, G.; Cheetham, A. K. *Science* **1999**, *283*, 1125−1126.

(15) Lu, G.; Li, S.; Guo, Z.; Farha, O. K.; Hauser, B. G.; Qi, X.; Wang, Y.; Wang, X.; Han, S.; Liu, X.; DuChene, J. S.; Zhang, H.; Zhang, Q.; Chen, X.; Ma, J.; Loo, S. C. J.; Wei, W. D.; Yang, Y.; Hupp, J. T.; Huo, F. *Nat. Chem.* **2012**, *4*, 310−316.

(16) Cadiau, A.; Adil, K.; Bhatt, P. M.; Belmabkhout, Y.; Eddaoudi, M. *Science* **2016**, *353*, 137−140.

(17) Cui, X.; Chen, K.; Xing, H.; Yang, Q.; Krishna, R.; Bao, Z.; Wu, H.; Zhou, W.; Dong, X.; Han, Y.; Li, B.; Ren, Q.; Zaworotko, M. J.; Chen, B. *Science* **2016**, *353*, 141−144.

(18) Doherty, C. M.; Buso, D.; Hill, A. J.; Furukawa, S.; Kitagawa, S.; Falcaro, P. *Acc. Chem. Res.* **2014**, *47*, 396−405.

(19) Silvestre, M. E.; Franzreb, M.; Weidler, P. G.; Shekhah, O.; Wöll, C. *Adv. Funct. Mater.* **2013**, *23*, 1210−1213.

(20) Lohe, M. R.; Gedrich, K.; Freudenberg, T.; Kockrick, E.; Dellmann, T.; Kaskel, S. *Chem. Commun.* **2011**, *47*, 3075−3077.

(21) Wang, G.-H.; Lei, Y.-Q.; Song, H.-C. *Anal. Methods* **2014**, *6*, 7842−7847.

(22) Ke, F.; Wang, L.; Zhu, J. *Nanoscale* **2015**, *7*, 1201−1208.

(23) Wang, Y.; Zhang, Y.; Hou, C.; Liu, M. *RSC Adv.* **2015**, *5*, 98260−98268.

(24) Zhao, X.; Liu, S.; Tang, Z.; Niu, H.; Cai, Y.; Meng, W.; Wu, F.; Giesy, J. P. *Sci. Rep.* **2015**, *5*, 11849.

(25) Jia, Y.; Su, H.; Wong, Y. L. E.; Chen, X.; Dominic Chan, T. W. *J. Chromatogr. A* **2016**, *1456*, 42−48.

DOI: 10.1021/acs.nanolett.7b03451
Nano Lett. 2017, 17, 6968−6973

(26) Li, L.; Wu, Y. Q.; Sun, K. K.; Zhang, R.; Fan, L.; Liang, K. K.; Mao, L. B. *Mater. Lett.* **2016**, *162*, 207−210.
(27) Li, W.; Li, G.; Liu, D. *RSC Adv.* **2016**, *6*, 94113−94118.
(28) Moradi, S. E.; Haji Shabani, A. M.; Dadfarnia, S.; Emami, S. *Anal. Methods* **2016**, *8*, 6337−6346.
(29) Wehner, T.; Mandel, K.; Schneider, M.; Sextl, G.; Müller-Buschbaum, K. *ACS Appl. Mater. Interfaces* **2016**, *8*, 5445−5452.
(30) Zhao, H.-X.; Zou, Q.; Sun, S.-K.; Yu, C.; Zhang, X.; Li, R.-J.; Fu, Y.-Y. *Chem. Sci.* **2016**, *7*, 5294−5301.
(31) Ke, F.; Jiang, J.; Li, Y.; Liang, J.; Wan, X.; Ko, S. *Appl. Surf. Sci.* **2017**, *413*, 266−274.
(32) Li, J.; Wang, J.; Ling, Y.; Chen, Z.; Gao, M.; Zhang, X.; Zhou, Y. *Chem. Commun.* **2017**, *53*, 4018−4021.
(33) Liu, P.; Liu, S.; Bian, S.-W. *J. Mater. Sci.* **2017**, *10*, 12121.
(34) Sun, X.; Gao, G.; Yan, D.; Feng, C. *Appl. Surf. Sci.* **2017**, *405*, 52−59.
(35) Akiyama, G.; Matsuda, R.; Sato, H.; Takata, M.; Kitagawa, S. *Adv. Mater.* **2011**, *23*, 3294−3297.
(36) Férey, G.; Mellot-Draznieks, C.; Serre, C.; Millange, F.; Dutour, J.; Surblé, S.; Margiolaki, I. *Science* **2005**, *309*, 2040−2042.
(37) Zhao, X.; Han, X.; Li, Z.; Huang, H.; Liu, D.; Zhong, C. *Appl. Surf. Sci.* **2015**, *351*, 760−764.
(38) Zhang, T.; Zhang, X.; Yan, X.; Kong, L.; Zhang, G.; Liu, H.; Qiu, J.; Yeung, K. L. *Chem. Eng. J.* **2013**, *228*, 398−404.
(39) Kelly, T. F.; Larson, D. J. *MRS Bull.* **2012**, *37*, 150−158.
(40) Devaraj, A.; Gu, M.; Colby, R.; Yan, P.; Wang, C. M.; Zheng, J.; Xiao, J.; Genc, A.; Zhang, J.; Belharouak, I. *Nat. Commun.* **2015**, *6*, 1 DOI: 10.1038/ncomms9014.
(41) Liu, J.-f.; Zhao, Z.-s.; Jiang, G.-b. *Environ. Sci. Technol.* **2008**, *42*, 6949−6954.
(42) Huo, J.; Aguilera-Sigalat, J.; El-Hankari, S.; Bradshaw, D. *Chem. Sci.* **2015**, *6*, 1938−1943.
(43) Li, H.; Sadiq, M. M.; Suzuki, K.; Ricco, R.; Doblin, C.; Hill, A. J.; Lim, S.; Falcaro, P.; Hill, M. R. *Adv. Mater.* **2016**, *28*, 1839−1844.
(44) Crocombette, J. P.; Pollak, M.; Jollet, F.; Thromat, N.; Gautier-Soyer, M. *Phys. Rev. B: Condens. Matter Mater. Phys.* **1995**, *52*, 3143−3150.
(45) Deng, H.; Li, X.; Peng, Q.; Wang, X.; Chen, J.; Li, Y. *Angew. Chem., Int. Ed.* **2005**, *44*, 2782−2785.
(46) Thompson, K.; Lawrence, D.; Larson, D. J.; Olson, J. D.; Kelly, T. F.; Gorman, B. *Ultramicroscopy* **2007**, *107*, 131−139.
(47) Brian P, Geiser; David J, Larson; Robert M, Ulfig; Thomas Forrest, Kelly; Prosa, T. J., Local Electrode Atom Probe Tomography: A User's Guide. In *Local Electrode Atom Probe Tomography: A User's Guide*; Springer: New York, 2013.

DOI: 10.1021/acs.nanolett.7b03451
Nano Lett. 2017, 17, 6968−6973